RSC Advances

PAPER

View Article Online
View Journal | View Issue

Check for updates

Cite this: *RSC Adv.*, 2022, **12**, 27826

Efficient fluorescent recognition of ATP/GTP by a water-soluble bisquinolinium pyridine-2,6-dicarboxamide compound. Crystal structures, spectroscopic studies and interaction mode with DNA†

Alejandro O. Viviano-Posadas, [a] Ulises Romero-Mendoza,[a] Iván J. Bazany-Rodríguez, [a] Rocío V. Velázquez-Castillo, [a] Diego Martínez-Otero, [b] Joanatan M. Bautista-Renedo,[b] Nelly González-Rivas, [b] Rodrigo Galindo-Murillo, [c] María K. Salomón-Flores [a] and Alejandro Dorazco-González [a]*

The new dicationic pyridine-2,6-dicarboxamide-based compound **1** bearing two *N*-alkylquinolinium units was synthesized, structurally determined by single-crystal X-ray diffraction, and studied in-depth as a fluorescent receptor for nucleotides and inorganic phosphorylated anions in pure water. The addition of nucleotides to **1** at pH = 7.0 quenches its blue emission with a selective affinity towards adenosine 5′-triphosphate (ATP) and guanosine 5′-tripohosphate (GTP) over other nucleotides such CTP, UTP, ADP, AMP, dicarboxylates and inorganic anions. On the basis of the spectroscopic tools (^{1}H, ^{31}P NMR, UV-vis, fluorescence), MS measurements and DFT calculations, receptor **1** binds ATP with high affinity (log K = 5.04) through the simultaneous formation of strong hydrogen bonds and π–π interactions between the adenosine fragment and quinolinium ring with binding energy calculated in 8.7 kcal mol^{-1}. High affinity for ATP/GTP is attributed to the high acidity of amides and preorganized rigid structure of **1**. Receptor **1** is an order of magnitude more selective for ATP than GTP. An efficient photoinduced electron transfer quenching mechanism with simultaneous receptor–ATP complexation in both the excited and ground states is proposed. Additionally, multiple spectroscopic studies and molecular dynamics simulations showed that **1** can intercalate into DNA base pairs.

Received 11th August 2022
Accepted 21st September 2022

DOI: 10.1039/d2ra05040d

rsc.li/rsc-advances

Open Access Article. Published on 29 2022. Downloaded on 03-08-2025 12:06:24.
This article is licensed under a Creative Commons Attribution-NonCommercial 3.0 Unported Licence.

Introduction

Selective recognition of nucleoside polyphosphates (NPPs) by luminescent molecular receptors remains an active and important area in supramolecular chemistry and analytical sciences[1–7] due to their key biochemical functions in genetic information and cellular energy transduction.[8] Among the NNPs, adenosine triphosphate (ATP) is the most abundant nucleotide in cells and is the primary chemical energy source in living systems.[9] On the other hand, guanosine triphosphate (GTP) regulates a wide variety of cellular processes ranging from protein synthesis, the citric acid cycle and RNA synthesis.[10] A variety of human illnesses such as kidney diseases, Alzheimer's, hypoglycemia and cancer are associated with deviations in ATP or GTP levels.[11–13] While the need for efficient and selective optical receptors for purine nucleotides (ATP/GTP) is evident, so far, few molecular receptors able to operate efficiently in neutral aqueous media at sub-micromolar concentrations have been described.

Fluorescent recognition of ATP/GTP has been dominated by organic artificial receptors containing arrays of hydrogen bond donors of NH/CH type or polycationic moieties as binding sites for the polyphosphate fragments.[14–24] Typically, these receptors show binding constants between 10^2 and 10^4 M^{-1}.[25,26] Consequently, they are suitable to recognize ATP/GTP in the millimolar concentration range, but not significantly below. These receptors also frequently require an organic cosolvent to operate, which seriously limits their intended applications.[14,27–31]

[a]*Institute of Chemistry, National Autonomous University of Mexico, Circuito Exterior, Ciudad Universitaria, México, D.F., 04510, Mexico. E-mail: adg@unam.mx; Tel: +52-55-56224514*

[b]*Centro Conjunto de Investigación en Química Sustentable UAEM-UNAM, km 14.5 Carrera Toluca-Atlacomulco, Campus UAEMex "El Rosedal" San Cayetano-Toluca, Toluca de Lerdo 50200, Estado de México, Mexico*

[c]*Department of Medicinal Chemistry, College of Pharmacy, University of Utah, 2000 East 30 South Skaggs 306, Salt Lake City 84112, Utah, USA*

† Electronic supplementary information (ESI) available: Crystallographic data, ^{1}H, ^{13}C, HMSQ, DEPT, MS measurements, atoms in molecules analysis and spectroscopic recognition studies. CCDC 2118468–2118469. For ESI and crystallographic data in CIF or other electronic format see https://doi.org/10.1039/d2ra05040d

© 2022 The Author(s). Published by the Royal Society of Chemistry

Open Access Article. Published on 29 2022. Downloaded on 03-08-2025 12:06:24.
This article is licensed under a Creative Commons Attribution-NonCommercial 3.0 Unported Licence.

Optical recognition of ATP or GTP by molecular hosts in water can be achieved with fluorescent imidazolium salts,[14,18,27] cyclophanes,[19,29] quinoline-based Zn-complexes,[3,32] lanthanide complexes[4] and bis- 2,6-formylphenol derivatives.[16] These luminescent receptors undergo changes in their photophysical properties due to the binding of the polyphosphate motif with the hydrogen bond donors or by coordination to the metal center.[33] However, in many cases they are not particularly selective towards purine nucleotides because their chemical structures only contain binding sites for the polyphosphate moieties.[7,34] Thus, interference from other nucleotides (CTP, UTP, TTP, ADP, AMP, GDP),[16,30,33,35] adenine dinucleotide (NADH)[36] and pyrophosphate (PPi)[34] can be a problem.

In principle, it should be possible to overcome these limitations by developing a fluorescent molecular receptor with specific, high-affinity, and cooperative binding points for ATP or GTP that includes hydrophilic fragments in its chemical structure. However, the creation of a potent, and selective receptor for GTP/ATP able to operate in a neutral aqueous phase is an ongoing challenge.[7] Recent reports in the context of oxyanion recognition have displayed that pyridine-2,6-dicarboxamide-based pincer receptors are able to bind phosphorylated anions through hydrogen bonds.[37] Previously, we reported a series of dicationic *N*-methylated bisquinolinium pyridine-2,6-dicarboxamide receptors with a moderate affinity towards PPi and ATP ranging between 300 and 5400 M^{-1} in water where the anion-binding is driven mainly by the acidification of the amide NH groups.[38]

On the hand, quinoline-based dyes as quaternary salts have found many applications in fluorescent molecular recognition of inorganic anions[39,40] and as pH-probes.[41] They have also been used as efficient DNA intercalators[42,43] and G-quadruplex ligands[44,45] where the supramolecular complex formed is stabilized by π-stacking interactions between π-electron-rich rings from guanine or adenine and the cationic aromatic π-electron-deficient ring from quinolinium.[46]

Taking this into account, we surmised that a sensitive optical recognition of ATP/GTP in water is possible with a combination of two binding sites based on a water-soluble pyridine-2,6-dicarboxamide cationic receptor with a high affinity for polyphosphate fragments and fluorescent quinolinium units as a cooperative binding site for purine rings *via* π–π interactions. The results obtained for a new nucleotide receptor **1** based on bisquinolinium pyridine-dicarboxamide including synthesis, crystal structure, acid–base properties, spectroscopic recognition studies and theoretical DFT calculations are summarized below. For comparison purposes, a related *N*-alkyl quinolinium benzamide derivative **2** lacking a polyphosphate binding site was also studied.

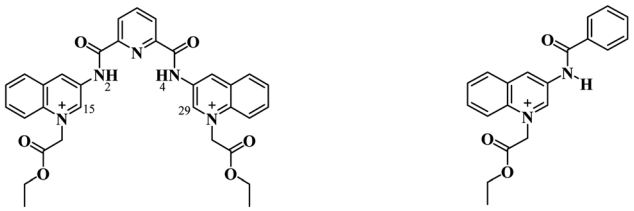

1 **2**

Scheme 1 Fluorescent receptors **1** and **2** employed in this study.

Results and discussion

Synthesis and crystal structures

Compounds **1** and **2** (Scheme 1) were successfully synthesized by the two-step procedure described in Scheme S1†.[47] The synthesis of **1** was initiated by reacting 2,6-pyridinedicarbonyl dichloride with 3-aminoquinoline in dry toluene, and subsequent prolonged treatment with ethyl bromoacetate in dry DMF.

The bromide salts of **1** and **2** were isolated in good yield as pale-yellow crystalline powders and pure according to ^{1}H, ^{13}C, DEPT, HSQC NMR spectroscopy (Fig. S1–S18†), and elemental analysis (C, N, H).

X-ray crystal structures were obtained for bromide salt of **1** and triflate salt of **2** by slow evaporation of methanolic solutions (see Table S1 in the ESI† for crystallographic data). Parameters for selected hydrogen bonding interactions within the crystal packing are collected in Tables S2–S3.†

Perspective views of molecular structures of **1** and **2** are shown in Fig. 1. Crystallographic analysis for **1** shows that it possesses a rather high degree of planarity: the dihedral angles between *N*-alkylated quinolinium rings and the central pyridine ring are $\varphi = 11.63$ and 22.78°. The two carboxamide groups are turned inside the cleft toward each other and are coplanar with the central pyridine ring, this *syn–syn* conformation has been commonly observed for crystal structures of pyridine-2,6-dicarboxamide derivatives for both macrocyclic[50–53] and acyclic species[30,34,38,39,47–51] as result of intramolecular hydrogen bonds between the central pyridine and the NH carboxamide groups.

Since the high planarity between the quinolinium rings and the carboxamide groups, the *ortho*-CH bonds from quinolinium rings show an optimal orientation towards the intracavity, therefore, **1** is a preorganized receptor with a well-defined cavity for recognition of anions. The distances NH···HN and *ortho*-(15) CH···HC(29) of **1** are 3.132 and 4.384 Å, respectively. The size of the cavity formed by NH and *ortho*-CH hydrogen bond donors is favorable for hosting halide ions[2] and phosphorylated anions, which induce a peak selectivity over other anions, as has been demonstrated in previous works.[52,53]

The carbon–nitrogen bond distance C_{sp^2}–$N_{sp^2} = 1.364(5)$ Å of the carboxamide groups in **1** is significantly longer than that found for neutral related derivatives in the range of 1.323–1.350 Å.[50]

This difference can be induced by the positive charges of lateral quinolinium moieties. The crystal of **1** is strongly hydrated with the consequence that the receptor cavity is occupied by a water molecule where the NH bonds of both carboxamide groups are oriented towards the oxygen atom from the water forming two N–H···O hydrogen bonds (Table S2†). It can be expected that a similar binding mode for tetrahedral anions such as phosphorylated-derivatives might occur also *via* charged-assisted N–H···$^{-}$O–P interactions.[48,51,52]

Crystal of **2** shows coplanarity between quinolinium and benzyl ring with a dihedral angle of $\varphi = 9.58°$, similar structural

Open Access Article. Published on 29 2022. Downloaded on 03-08-2025 12:06:24.
This article is licensed under a Creative Commons Attribution-NonCommercial 3.0 Unported Licence.

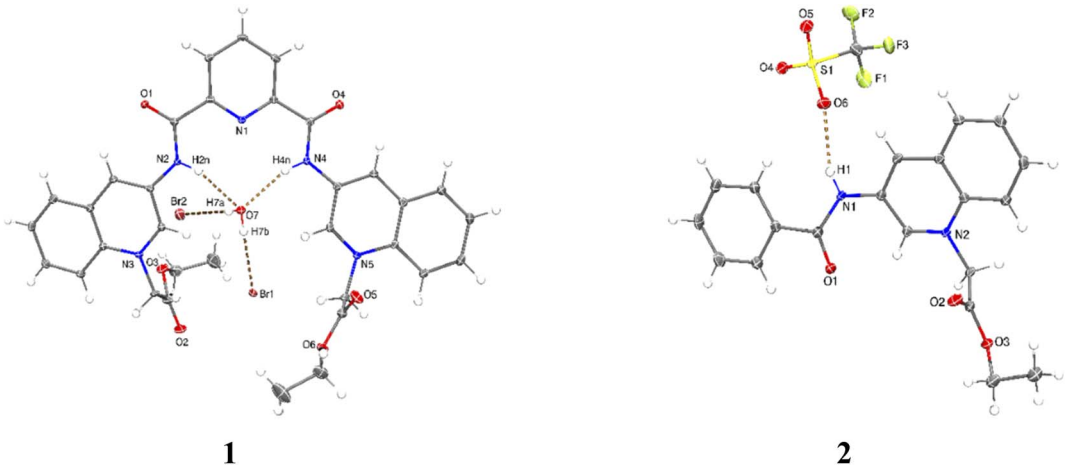

1 2

Fig. 1 Perspective views of molecular structures of bromide salt of **1** (additional water and methanol molecules were omitted for clarity) and triflate salt of **2**. Ellipsoids are drawn at the 30% probability level.

properties have been reported previously for a benzamide derivative.[54] The positive charge of **2** is stabilized by a triflate *via* N–H···O interactions (Table S3†).

Optical and acid–base properties

Acid–base properties of bromide salts of **1** and **2** were studied by UV-vis and fluorimetric pH-titrations. Absorption and emission maxima in water at pH = 7.0 are collected in Table 1 and the family of spectra at different pH values are compiled in Fig. 2. In *N*-alkylquinolinium salts, the long-wavelength absorption band near 350 nm is typically attributed to n → π* electronic transitions[55] and the blue/green fluorescence is originated by intramolecular charge transfers (ICT) in the excited state.[56]

Buffered aqueous solutions (10 mM MOPS, pH = 7.0) of bromide salts of **1–2** were stable for several days and followed very well to the Lambert–Beer law up to 50.0 μM, thus these conditions were used for further studies.

On increasing pH, the absorbance at shorter wavelengths (~275 nm) decreases while at longer wavelengths it increases (~350 nm) and the blue emission is strongly quenched for both salts. For **2**, spectrophotometric titration experiment (Fig. 2B) shows three clear isosbestic points at 282, 330 and 360 nm indicating the chemical equilibrium between the protonated/deprotonated species of the amide group.

In the case of **1**, two processes are observed (Fig. 2A), the first one given in the pH range 6.0–8.[61] by a sharp decrease in absorbance at the maximum 276 nm with three isosbestic points at 302, 335, and 369 nm. The second process at pH > 8.8 with an increase in absorbance at longer wavelengths. The pK_a values calculated are shown in Table 1.

In general, the acid-base dissociation constants are significantly lower than those typical for common amides due to the combination of the strong electron-accepting properties of the central pyridyl ring and the positive charge on quinolinium rings. The absence of the electron-accepting effect by the pyridyl ring in **2** is reflected in a higher pK_a value closer to ordinary amides. Species with deprotonated carboxamide groups in **1** and **2** are practically not fluorescent by an intramolecular photoinduced electron transfer (PET) caused by deprotonation in the excited state, forming a non-emitting conjugated base.[38]

The pK_a values of **1** calculated by fluorescence spectroscopy are slightly lower than those calculated by UV-vis suggesting a contribution of the excited state deprotonation (Table 1).

Taking into account the fluorescence emission, the high acidity of the amide groups, the preorganization of the NH/CH donors, and the dicationic nature of water at pH = 7.0 of **1**, we explored this compound as a receptor for a series of phosphorylated anions by experimental and theoretical studies.

NPPs recognition studies

The first evidence for the high affinity of ATP/GTP for **1** was obtained by ^{31}P and ^{1}H NMR measurements. The phosphate binding modes of sodium salts of ATP/GTP with **1** were investigated by ^{31}P NMR spectroscopy in neutral D_2O solutions (Fig. 3). The free ATP has signals at −10.77 (γ-P), −11.21 (α-P), and −22.93 (β-P) and the addition of 1.0 equiv. of **1** induces

Table 1 Absorption and emission maxima (nm) and pK_a values of **1** (10 μM) and **2** (10 μM) in water

		UV-vis		Emission	Fluorimetric titration	
	λ_{abs} (log ε) (pH = 7.0)	pK_{a1}	pK_{a2}	(λ_{exc} = 350 nm)	pK·	pK_{a2}
1	276(4.43), 350(3.90)	7.70 ± 0.02	10.10 ± 0.09	415	7.12 ± 0.03	9.23 ± 0.05
2	270(4.16), 346(3.73)	10.57 ± 0.02	—	410	10.37 ± 0.04	—

© 2022 The Author(s). Published by the Royal Society of Chemistry

Open Access Article. Published on 29 2022. Downloaded on 03-08-2025 12:06:24.
This article is licensed under a Creative Commons Attribution-NonCommercial 3.0 Unported Licence.

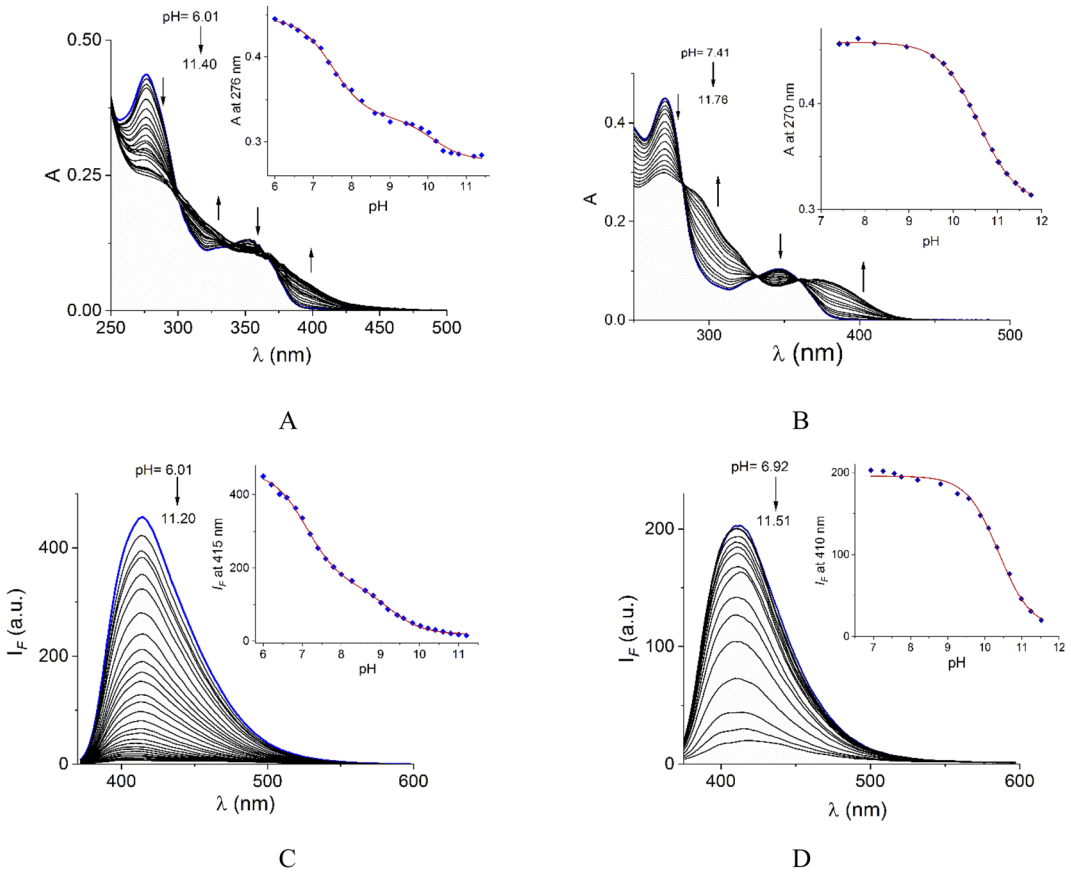

Fig. 2 UV-vis pH-titrations of buffered aqueous solutions (10 mM MOPS and CAPS) of **1** (A) and **2** (B) at 25 °C. Fluorescence (λ_{ex} = 350 nm) pH-titrations of buffered aqueous solutions of **1** (C) and **2** (D) at 25 °C. The insets show pH-titration profiles observed at absorbance and emission maxima.

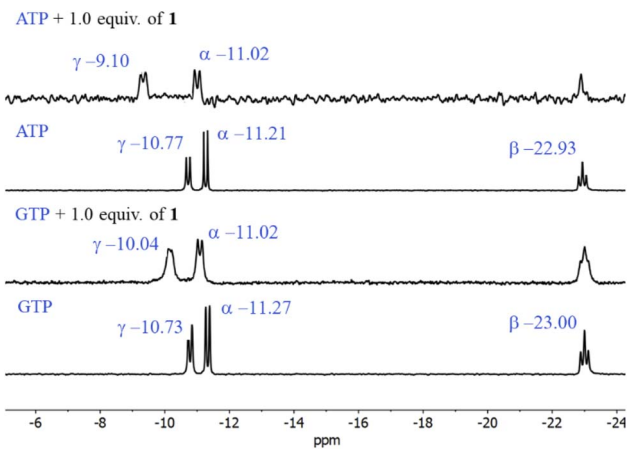

Fig. 3 Partial ^{31}P NMR spectra (121.5 MHz, 25 °C) of sodium salts of ATP and GTP (3.0 mM) in the presence of 1.0 equiv. of **1** in D_2O at pD = 7.0 (10 mM MOPS).

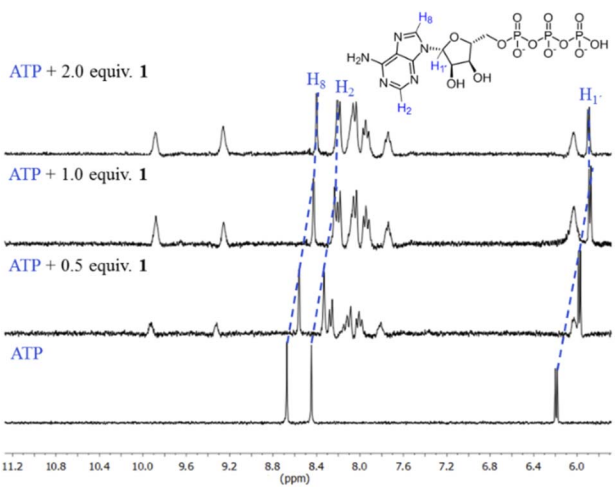

Fig. 4 Partial ^{1}H NMR spectra (400 MHz, 25 °C) of sodium salt of ATP (3.0 mM) + **1** (0.5, 1.0, 2.0 equiv.) in D_2O at pD = 7.0 (10 mM MOPS). Blue dotted lines show upfield shifting in H_8, H_2 and $H_{1'}$ protons of the adenosine ring.

a considerable broadening of terminal γ-P signal with evident downfield shift ($\Delta\delta$ = 1.67 ppm) which can be assigned to the formation of N–H···O–P-γ hydrogen bonds. The nature of this shift can be ascribed to a "partial protonation" of the γ-P phosphate as would be expected by the interaction with the NH carboxamide groups. In the case of GTP, the shift of γ-P signal was significantly lower than that observed for ATP. Similar NMR spectroscopic changes, in particular, the downfield shift of ^{31}P-

Open Access Article. Published on 29 2022. Downloaded on 03-08-2025 12:06:24.
This article is licensed under a Creative Commons Attribution-NonCommercial 3.0 Unported Licence.

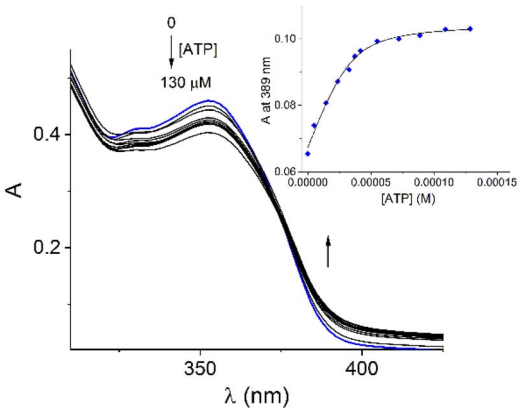

Fig. 5 Spectrophotometric titration experiment of buffered aqueous solution of **1** (40 μM) upon the addition of increasing amounts of ATP at pH = 7.0 (10 mM MOPS, 25 °C). Inset: shows the profile of absorbance at 389 nm for increasing amounts of ATP. The solid lines were obtained by fitting the experimental data to a 1 : 1 model. The ionic strength was adjusted to 0.05 M of NaCl.

signals have been observed with organic polyammonium-based receptors and they are assigned to the formation of strong hydrogen bonds.[57] To gain further information regarding the interaction of adenosine fragment to quinolinium rings, ^{1}H NMR experiments were performed. Fig. 4 shows the aromatic region of ^{1}H NMR spectra of free ATP and with increasing amounts of **1**. Clearly, protons of adenine H_2, H_8 and proton of ribose fragment H_1 undergo significant upfield shifts by 0.31–0.58 ppm indicating interactions between adenosine moiety and **1**.

Such ^{1}H NMR spectral changes have been observed in supramolecular-complexes of ATP with receptors derivatives of acridine-appended polyammonium as a result of π-stacking interactions.[22] Reports in the context of ATP-binding proteins have shown that aromatic amino acids drive the binding with the adenosine ring inducing selectivity over the rest of the NPPs.[58]

There are several examples of receptors for ATP recognition containing aromatic groups linked to polyammonium groups operating through electrostatic and π-stacking interactions with the adenosine ring typically at acid pH.[7,22] A new property of receptor **1** is that it provides two simultaneous two-point recognition capable of operating in neutral pure water as observed in NMR experiments.

Addition of ATP and GTP to buffered aqueous solutions of **1** at pH = 7.0 induced small, but clearly observed changes in UV-vis spectra. As an example, Fig. 5 displays the family of UV-vis spectra obtained when a neutral aqueous solution of **1** is titrated with ATP. The inset shows the increase of absorbance at 389 nm on the progressive addition of ATP. This profile remained practically unchanged when the **1**/ATP ratio reached 1.0 equiv. The variation in the absorbance ($\Delta A \sim 0.05$) at 389 nm with increasing ATP concentration fits perfectly to 1 : 1 stoichiometric model with a binding constant of $\log K = 4.94 \pm 0.11$. An isosbestic point at 374 nm is observed, which suggests that only two species are in equilibrium (free **1** and its complexed form with ATP). The mass spectrum of **1** in the presence of 1.0 equiv. of ATP by a positive scan of ESI showed practically one species at 652.06 m/z, which was isotopically resolved, and it can be assigned to the dicationic complex 1 : 1, $\{\mathbf{1}^{2+} + ATP^{2-} + Br^- + 3Na^+ + 2H_2O\}^{2+}$ (676.6 m/z). The experimental signals, separated by 0.5, match well the theoretical isotopic distribution for a complex 1 : 1, ATP : **1** as is shown in Fig. S20.† These experiments unambiguously confirm the binding of ATP with **1** in neutral water.

In contrast to UV-vis measurements, fluorescence experiments provided strong and reproducible changes of **1** by additions of NPP_S. Thus, the interaction of receptors **1**–**2** with several NPPs and PPi were studied by fluorimetric titration experiments under the same conditions. Next, the addition of ATP and GTP to an aqueous solution of **1** induced a strong quenching as is shown in Fig. 6A and S19.†

The Stern–Volmer (S–V) plot at 415 nm ($\lambda_{ex} = 350$ nm) with increasing ATP concentration up to 65 μM shows a clear downward curved profile. This curve shape is typically observed by a combination of static and dynamic quenching. This profile can be very-well fitted to the theoretical eqn (1) proposed by Fabbrizzi[59] which takes into account simultaneous static and dynamic quenching when the ground state complexation does not quench the emission completely and the receptor–guest complex still possesses a residual fluorescence intensity (factor ρ).

$$\frac{I_0}{I} = (1 + K_{SV}[\text{anion}])(1 + K_A[\text{anion}])/\ (1 + \ \rho K_A[\text{anion}]) \quad (1)$$

The estimated binding constant ($\log K_{(ATP)} = 5.01 \pm 0.03$) for static quenching is consistent with that obtained by UV-vis, indicating that complexation is mainly formed in the ground state. High affinities of **1** towards ATP/GTP ($\log K_{(ATP)} = 5.01 \pm 0.03$ and $\log K_{(GTP)} = 4.70 \pm 0.05$) can be attributed to the cooperative two-point recognition which was supported by NMR experiments.[47]

S–V plots for ATP, GTP, CTP, UTP, ADP and AMP are shown in Fig. 6B. In general, titrations for all NPPs show non-linear profiles similar to ATP and GTP with downward curves but with a small quenching effect at saturation.

The calculated parameters corresponding to binding constant with 1 : 1 stoichiometry (K_A), dynamic quenching constant (K_{SV}) and residual factor ρ using eqn (1) for NPPs and PPi are listed in Table 2.

Eqn (1) is approximate because it considers similar quenching with a single K_{SV} value for both free and complexed forms of the fluorophore as well as similar rates of photoexcitation of free and its complexed form. A more exact equation was described by Boens,[60] however, it includes many adjustable parameters, which cannot be reliably determined from the fitting of plots as those shown in Fig. 6. Another limitation of eqn (1) is that if the static quenching is very strong, the estimated K_{SV} values may have large errors including values of dynamic quenching rate constants (K_q) that can exceed 100% of the upper diffusion limit for dynamic quenching in water which is physically impossible.

© 2022 The Author(s). Published by the Royal Society of Chemistry

Open Access Article. Published on 29 2022. Downloaded on 03-08-2025 12:06:24.
This article is licensed under a Creative Commons Attribution-NonCommercial 3.0 Unported Licence.

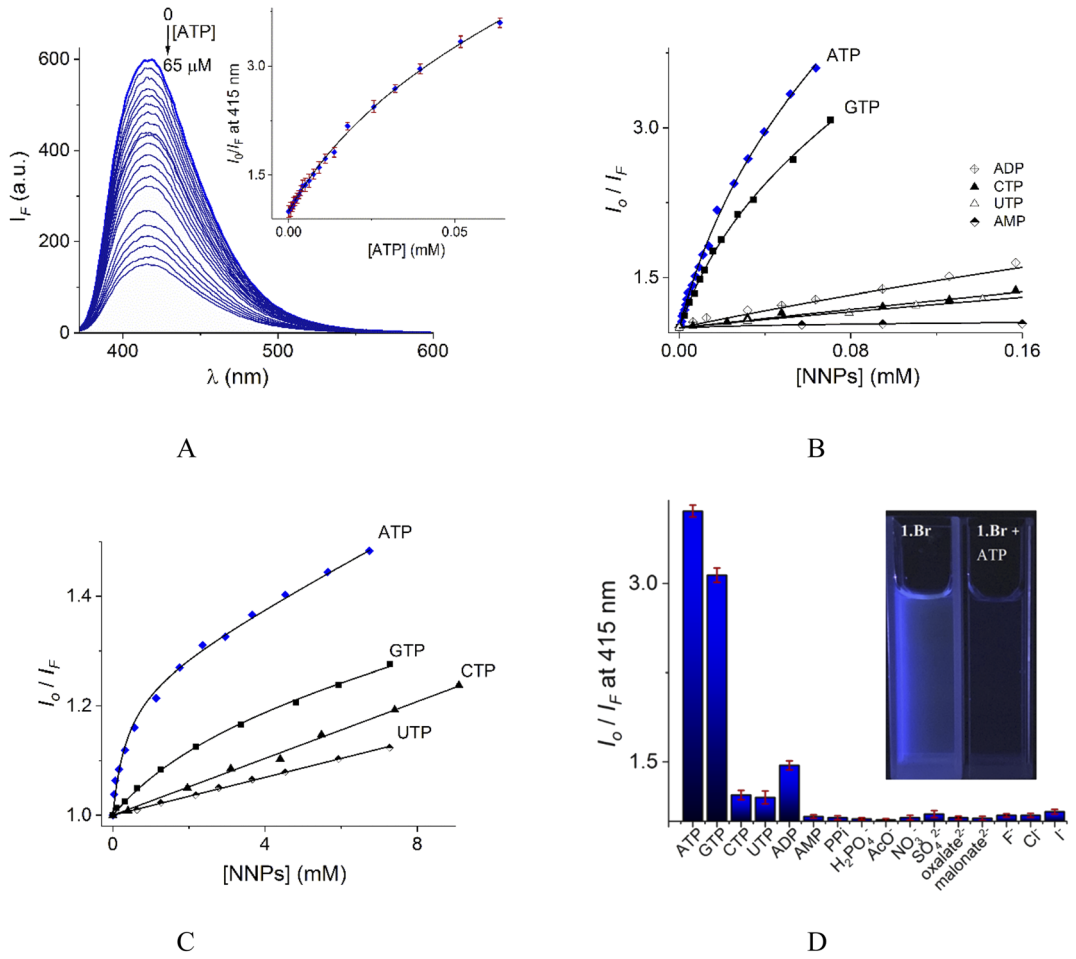

Fig. 6 (A) Changes of emission spectra (λ_{ex} = 350 nm) of buffered aqueous solutions at pH = 7.0 (10 mM MOPS) of **1** (12 μM) upon addition of increasing amounts of ATP at 25 °C. The inset shows the S–V plot at 415 nm. The solid line was obtained by fitting to eqn (1). S–V plots for fluorimetric titration experiments of **1** (B) and **2** (C) (λ_{ex} = 350 nm, emission at 415 and 410 nm for **1** and **2** respectively) with a series of NNPs at pH = 7.0. (D) The fluorescence quenching at 415 nm of aqueous solution of **1** upon additions of different anions as sodium salts (0.50 mM), average of triplicate experiments.

Fig. 6D illustrates anion selectivity of **1** at a single wavelength in terms of the fluorescence quenching (I_o/I_F) induced by additions of different nucleotides, oxyanions and halides ($[X^-]_{total}$ = 0.50 mM). In general, inorganic anions, dicarboxylates, pyrimidine nucleosides, ADP and AMP gave a very low response. The addition of GTP resulted in a considerable quenching in emission intensity, but it was still lower than that observed for ATP. This quenching effect by ATP/GTP addition is not unexpected because it is well-known that fluorescent aromatic rings with electron deficiency as quinolinium rings

Table 2 Binding and quenching constants for receptors **1** and **2** with NPPs and PPi at pH 7.0

	1				**2**			
	log K_A	log K_{SV}	ρ	I_o/I^a	log K_A	log K_{SV}	ρ	I_o/I
ATP	5.01 ± 0.03	3.57 ± 0.02	0.24	3.61	3.13 ± 0.09	1.41 ± 0.02	0.78	1.08
GTP	4.70 ± 0.05	3.32 ± 0.03	0.30	3.07	2.54 ± 0.10	1.38 ± 0.05	0.85	1.05
CTP	3.46 ± 0.08	2.70 ± 0.06	0.40	1.22	—	1.39 ± 0.08[b]	—	1.04
UTP	3.35 ± 0.09	2.59 ± 0.10	0.50	1.20	—	1.23 ± 0.10[b]	—	1.03
ADP	3.77 ± 0.09	2.79 ± 0.10	0.33	1.47	—	[c]	—	—
AMP	3.16 ± 0.11	1.30 ± 0.04	0.70	1.04	—	[c]	—	—
PPi	2.57 ± 0.07	1.25 ± 0.07	0.74	1.03	—	[c]	—	—

[a] I_o/I indicates the relative quenching parameter of the fluorescence intensity at 415 and 410 nm of **1** (10 μM) and **2** (10 μM) respectively in the presence of 0.1 mM of the corresponding NPPs. [b] These data were fitted to classic Stern–Volmer eqn (2). [c] not calculated.

Open Access Article. Published on 29 2022. Downloaded on 03-08-2025 12:06:24.
This article is licensed under a Creative Commons Attribution-NonCommercial 3.0 Unported Licence.

have a strong luminous quenching ability when they are bound to anions through a photoinduced electron transfer (PET) process. Fitting of the S–V plots (Fig. 6C) of **2** with ATP and GTP, gives small binding constants (Table 2) with values of ~2 orders of magnitude lower than those estimated for **1**. CTP and UTP showed no association with **2** and their profiles can be fitted to the classic linear Stern–Volmer equation indicating only dynamic quenching. The binding constant of **1** towards ATP is better than most previously reported water-soluble receptors bearing dicarboxamide groups as binding sites.[35,62–66]

DFT studies

To gain further insight into the recognition mode of **1** towards ATP/GTP density functional theory calculations were carried out. Final structures of 1 : 1 complexes between ATP/GTP and **1** are presented in Fig. 7.

These structures show the presence of strong hydrogen bond interactions between terminal phosphate groups of the nucleotides and NH carboxamide groups of **1**, while the nucleotide aromatic ring interacts with a quinolinium group of **1** across π–π interactions. These calculations are consistent with those observed by NMR experiments.

Interaction energy estimated for all nucleotide bases, presented in Table S4†, shows the affinity order ATP ~ GTP > CTP > UTP, where ATP is the nucleotide with the highest affinity (E_{int} = −40.30 kcal mol^{-1}), and UTP (E_{int} = −22.50 kcal mol^{-1}) is the nucleotide with the lowest affinity for **1**. The difference in affinities can be explained in terms of the π–π surface interaction between purine rings and **1**, represented by NCI plot, Fig. 8. Clearly, the complexes with the largest interaction surface show the best interaction energies. On the basis of experimental studies and DFT calculations, the chemical equilibrium of the ATP recognition by **1** is shown in Scheme 2.

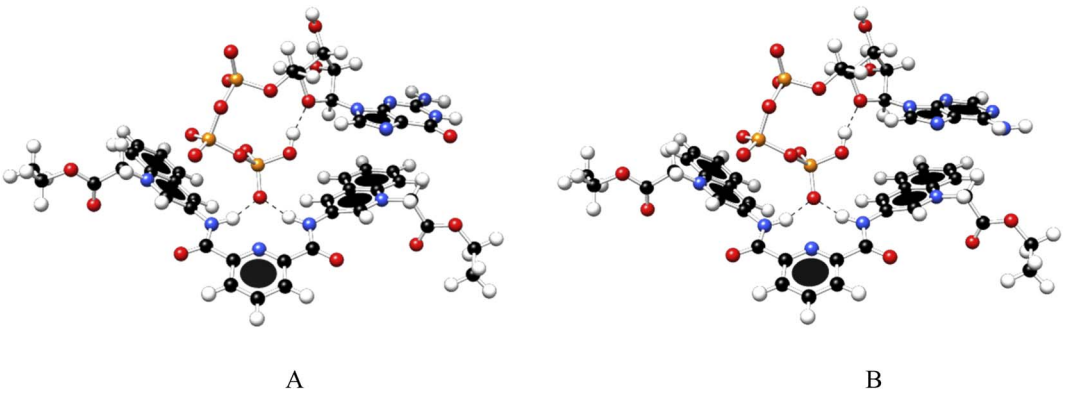

Fig. 7 Optimized structures of 1 : 1 complex of ATP (A) and GTP (B) with **1**, obtained at the PBEh-3c method.

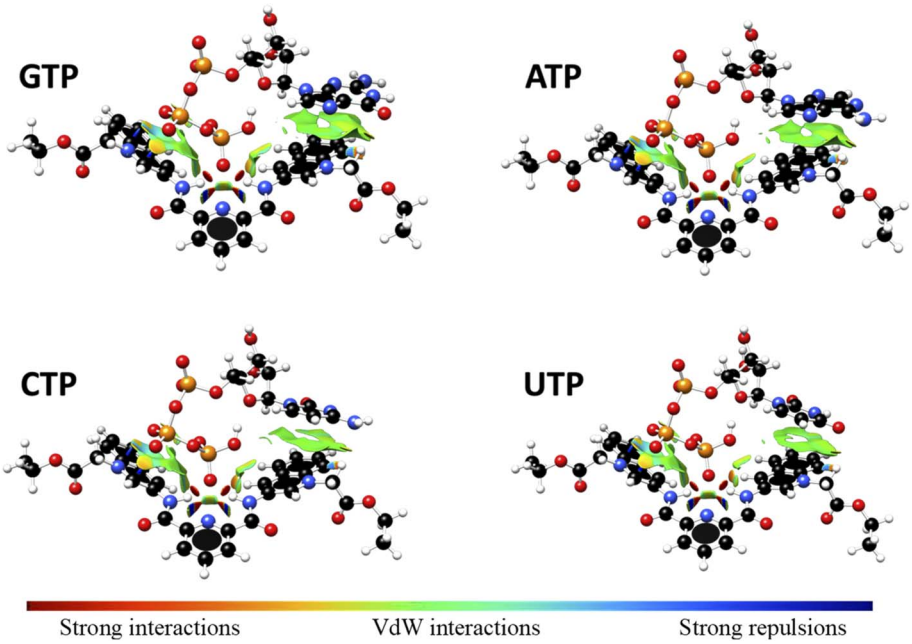

Fig. 8 Non-Covalent-Interactions-Index of GTP : **1**, ATP : **1**, CTP : **1** and UTP : **1** supramolecular complexes, obtained at the PBEh-3c method.

© 2022 The Author(s). Published by the Royal Society of Chemistry

Open Access Article. Published on 29 2022. Downloaded on 03-08-2025 12:06:24.
This article is licensed under a Creative Commons Attribution-NonCommercial 3.0 Unported Licence.

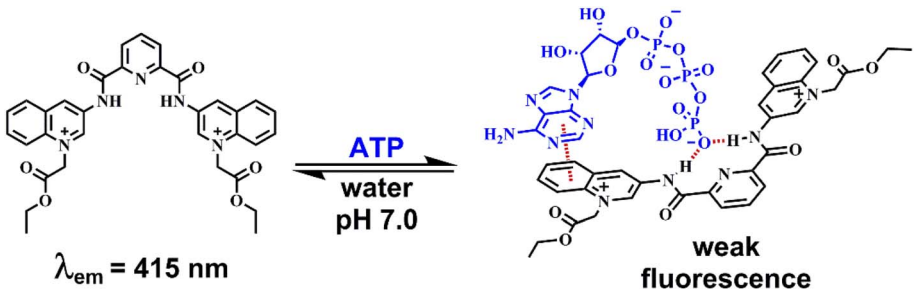

Scheme 2

Exploring interaction mode of 1 with DNA

The binding of **1** to DNA was also explored by spectroscopic titrations and molecular docking simulations. The binding mode can be preliminarily inferred by UV-vis measurements when comparing the effect of DNA on the absorption spectrum of **1** with the effect of a well-known standard DNA intercalator such as ethidium bromide (EB).[67]

UV-vis spectra of **1** upon increasing amounts of DNA in aqueous solutions at pH = 7.0 are shown in Fig. S21A.† The absorption peak of **1** at 350 nm decreases by the addition of DNA with a considerable bathochromic effect ~14 nm, additionally, one isosbestic point at 369 nm was observed. Typically, these red-shift and hypochromic effects are spectral changes when small molecules intercalate with DNA.[68] For example, EB is a potent intercalating agent for DNA and the supramolecular complex formed is stabilized by π–π stacking interactions. The effect of DNA on the absorption spectrum of EB under the same conditions of **1** is shown in Fig. S21B.† The addition of DNA to aqueous solutions of **1** and EB induced similar absorption changes suggesting intercalation of **1** with DNA. It is well documented that the structural changes of quinolinium derivatives induced by intercalation with DNA reduce the π–π* transition energies resulting in a hypochromic effect.[45,68]

To verify the interaction of **1** with DNA, steady-state competitive titration experiments were conducted using EB as a fluorescent indicator/intercalator. In the presence of DNA, EB emits at 605 nm due to its efficient intercalation between the adjacent DNA base pairs. In contrast, free EB has a very weak emission as is shown in Fig. 9A.

This displacement assay is based on the quenching of emission resulting from the displacement of EB by an intercalator molecule, where the quenching effect is due to the reduction of the number of binding sites on the DNA that are available to the EB.[68–70]

The family of spectra of DNA-bound EB in the absence and the presence of increasing amounts of **1** at 25° is given in Fig. 9A. There is a significant reduction in the emission intensity about of 77% at saturation of **1**. These results indicate that the DNA-bound EB is partially replaced by **1** and the molecules of **1** intercalate into DNA, which is consistent with the above results obtained by UV-vis.

The nature of this quenching effect can be quantitatively analyzed by the linear Stern–Volmer eqn (2).[69]

$$\frac{I_o}{I_F} = 1 + K_q\tau_o[Q] = 1 + K_{SV}[Q] \quad (2)$$

where I_o and I_F are the fluorescence intensities in the absence and presence of **1**. In this medium, the quencher is **1** and $[Q]$ indicates the concentration of **1**. K_{SV} expresses the S–V quenching constant and it is determined by linear regression of the plot of I_o/I_F against $[Q]$ (Fig. 9B). K_q is the DNA-bound EB

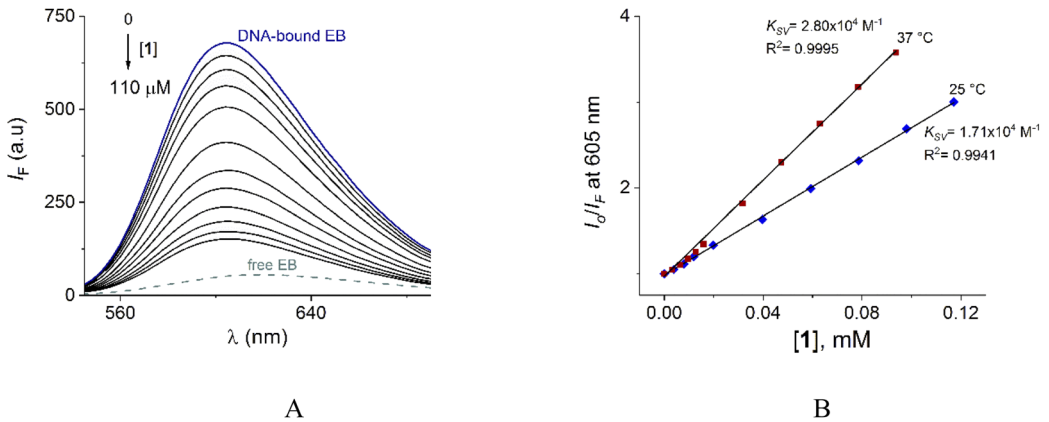

Fig. 9 (A) Fluorescence spectra (λ_{ex} = 520 nm) of DNA–EB upon the addition of increasing amounts of **1** at pH = 7.0 (10 mM MOPS, 25 °C). DNA and EB total concentrations are 250 μM and 50 μM, respectively. The ionic strength was adjusted to 50 mM of NaCl. (B) S–V plots for the quenching of system DNA–EB by **1** at 25 and 37 °C.

Open Access Article. Published on 29 2022. Downloaded on 03-08-2025 12:06:24.
This article is licensed under a Creative Commons Attribution-NonCommercial 3.0 Unported Licence.

Table 3 **1**-DNA–EB complex interaction parameters; quenching constants (K_{SV}), quenching rate constant (K_q), binding constants (K_A) and binding site numbers (n) at different temperatures

T (°C)	log K_{SV}	$K_q \times 10^{12}$ (Lmol^{-1} s^{-1})	R^{2a}	log $K_{A(DNA-1)}$	n	R^{2b}
25	4.22	1.71	0.9994	4.42	1.06	0.9983
37	4.45	2.80	0.9995	4.88	1.13	0.9986

[a] R^2 (K_{SV}). [b] R^2 ($K_{A(DNA-1)}$ and n) are the correlation coefficients.

complex quenching rate constant, τ_o is the average lifetime of fluorophore in the absence of **1** and its value is 10^{-8} s (taken from literature).[69]

The quenching process is classified into two types: dynamic and static quenching. Dynamic quenching is a collisional quenching and an increase in quenching rate constant values (K_q; $K_{SV} = K_q\tau_o$) with the increase in temperature is distinctive for this process due to increasing the temperature results in a higher diffusion coefficient. The upper K_q limit value for a dynamic quenching is 2.0×10^{10} L mol^{-1} s^{-1}.[68,69]

Next, the nature of the quenching of system DNA–EB by **1** was inferred by comparison of the behavior of the S–V plots at different temperatures (Fig. 9B). K_q values for the studied system were 1.70×10^{12} and 2.80×10^{12} Lmol^{-1} s^{-1} at 25 and 37 °C (Table 3). The increase of K_q and K_{SV} values at higher temperatures supports the dynamic quenching processes between system EB and **1**. However, the values of K_q are larger than the upper value for dynamic quenching which indicates a contribution of static quenching.[68,70,71] Thus, the quenching mechanism of system DNA–EB with **1** can be interpreted as a combined quenching process.

Considering hypothetically that the static binding quenching between DNA and **1** takes place with similar and independent binding sites, the binding constant (K_A) and the number of binding sites (n) can be determined by Scatchard eqn (3).[68]

$$\log\frac{I_o - I_F}{I_F} = \log K_A + n\log[Q] \quad (3)$$

K_A and n values were obtained from the intercept and slope of the linear plot of $\log(I_o - I_F)/I_F$ *versus* log [Q] (Fig. S22†) respectively and shown in Table 3. At 25 °C, K_A value indicated that **1** is tightly bound to DNA in the micromolar concentration range. The number of binding sites was obtained to be 1.06, indicating 1 : 1 stoichiometry between **1** and DNA.

On the other hand, it is known that the secondary structure of DNA can be modified by the intercalation of small molecules, and this structural change can be detected by circular dichroism. If the CD-spectrum strongly changes by the addition of a small molecule, confirms an intercalative binding process.[71] Otherwise, when the spectrum remains unchanged, indicates groove binding or simple electrostatic interactions.[72] Compound **1** was added to DNA neutral aqueous solution and the CD spectra were recorded. As shown in Fig. S22,† the negative and positive peaks at 242 nm and 282 nm of DNA increase their intensities by adding **1** with a slight shift of the maxima at higher wavelengths. These observed results are consistent with an intercalative binding of **1** with DNA.

Molecular dynamics simulation

Finally, to study the modes of interaction of **1** with a segment of double-stranded DNA, we used the 28-mer palindromic sequenced (CATGCATGCATGCATGCATGCATGCATG). The reduce any bias with regards of the interaction of the molecules with the DNA, three copies of **1** where manually placed near the center of the DNA using a distance of 10 Å from the helical center (Fig. 10).

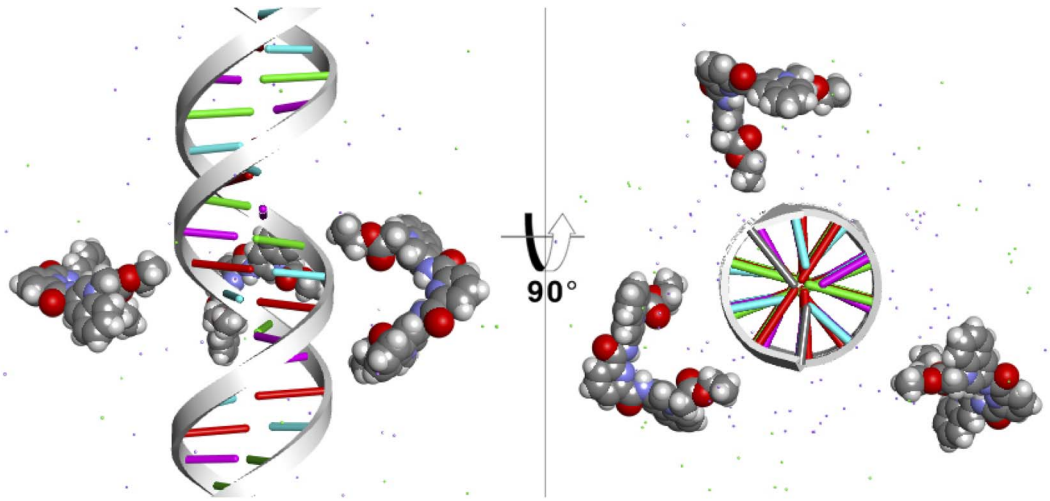

Fig. 10 Starting position of the MD simulations. Three molecules of **1** were places at 10 Å from the helical center of the 26-mer.

© 2022 The Author(s). Published by the Royal Society of Chemistry

Open Access Article. Published on 29 2022. Downloaded on 03-08-2025 12:06:24.
This article is licensed under a Creative Commons Attribution-NonCommercial 3.0 Unported Licence.

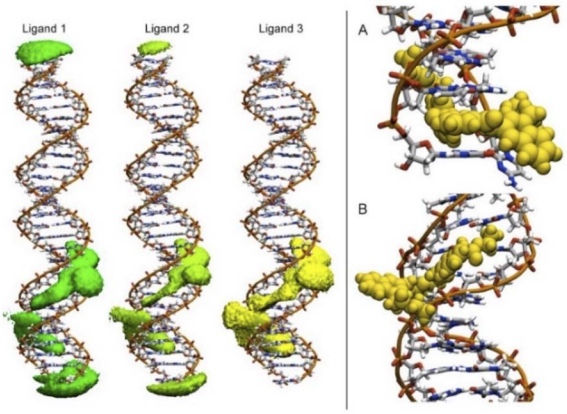

Fig. 11 Most populated position of each of the three independent molecules of ligand **1** present in the simulations (left). Representative modes of interaction of **1** with DNA (right).

To detect the interactions of each ligand from the MD simulations, a 3D-histogram was constructed using the entire 36 μs of sampling time calculated. The 3D-histogram grid (depicted in Fig. 11) shows the most populated position of each of the three independent molecules present in the simulations. It is clear that two of the molecules of **1** form a stacking interaction with the terminal base pairs of the DNA for the entire MD simulation. When the molecules are not forming interactions with the bases at the ends of the DNA, they explore different conformations which, suggesting by the 3D histogram, the main mode of interaction is minor groove binding within one of the CATG regions. In Fig. 11, panel A we can observe a representative mode of interaction in the 5′ terminal base-pairs with **1** forming an intercalation type of binding mainly formed between the aromatic rings of the A/T base-pairs and the aromatic rings of **1**. In the same figure, panel B we can observe the minor groove type of interaction that is formed between the aromatic rings of **1** and the back-bone of the DNA.

Conclusions

The dicationic derivative *N*,*N*-bis(*N*-alkylquinolinium)pyridine-2,6-dicarboxamide **1** can be used as a fluorescent receptor for purine nucleotides in neutral aqueous solution in the micromolar concentration range with good selectivity over other nucleoside polyphosphates and phosphorylated inorganic anions.

At pH = 7.0, the addition of nucleoside polyphosphates quenches the blue-emission of **1** with the highest efficiency for ATP, which displays highly selective recognition ($\log K_A = 5.01$). The quenching process could be explained by a static ATP-complexation PET mechanism possibly in both the excited and the ground state.

The crystal structure of **1**, NMR spectroscopic experiments and DFT calculations showed that ATP is bound to **1** through two cooperative binding points involving: (1) strong hydrogen bonds of the type N–H···O–P(γ), driven by the high acidity of the amide groups and preorganization of the receptor **1**, and (2) stacking interactions between π-electron-rich ring from adenine and the aromatic π-electron-deficient ring from quinolinium.

Furthermore, multiple spectroscopic studies and molecular dynamics simulations showed that **1** can intercalate into DNA base pairs with a binding constant of $\log K_{A(DNA-1)} = 4.98$.

Overall, these results further highlight the utility of pyridine-2,6-dicarboxamide-based preorganized pincer receptors bearing fluorescent units for supramolecular analytical applications.

Experimental section

General considerations

Chemicals, solvents and instrumentations are listed in ESI†.

Chemical synthesis

Compound **1** and **2** were prepared according to a modified procedure reported previously.[47] The detail procedure is described in ESI†.

3,3′-((Pyridine-2,6-dicarbonyl)bis(azanediyl))bis(1-(2-ethoxy-2-oxoethyl)quinolin-1-ium) bromide, 1. ^{1}H-NMR (400 MHz, DMSO-d_6) δ = 12.12 (s, 2H), 10.39 (d, J = 2.40 Hz, 2H), 9.89 (d, J = 1.36 Hz, 2H), 8.62–8.57 (m, 4H), 8.50 (dd, $^3J_{HH}$ = 8.52 Hz, $^3J_{HH}$ = 6.96 Hz, 1H, 8.45 (d, J = 9.16 Hz, 2H), 8.23 (td, J = 8.42, 1.00 Hz, 2H), 8.08 (t, J = 7.59 Hz, 2H), 6.36 (s, 4H), 4.28 (q, J = 7.10 Hz, 4H), 1.28 (t, J = 7.08 Hz, 6H). ^{13}C-NMR (125 MHz, DMSO-d_6) δ 166.10, 162.60, 147.59, 145.92, 141.03, 137.58, 135.75, 134.90, 132.25, 130.50, 130.34, 129.21, 126.72, 118.86, 62.58, 57.99, 14.01. MS (ESI$^+$) m/z = 673.7, Calcd. [$C_{33}H_{31}O_6N_5Br^+$ = 673.14]. IR (ATR) 3304.18*w* (N–H), 2975.58w (C–H_{arom}), 1742.64*m* (C═O), 1675.32*m* (N–H), 1545.42*m* (N–H), 1371.41*m* (–CH_3), 1203.64*m* (C–O). Anal. Calcd. For $C_{33}H_{31}Br_2N_5O_6$: C, 52.61; H, 4.15; N, 9.30. Found: C, 52.53; H, 4.27; N, 9.14.

3-Benzamido-1-(2-ethoxy-2-oxoethyl)quinolin-1-ium bromide, 2. ^{1}H-NMR (300 MHz, DMSO-d_6) = δ 11.43 (s, 1H), 10.04 (d, J = 2.22 Hz, 1H), 9.45 (d, J = 2.3 Hz, 1H), 8.53 (dd, $^3J_{HH}$ = 8.30, $^4J_{HH}$ = 0.88 Hz, 1H), 8.40 (d, J = 8.96 Hz, 1H), 8.18 (ddd, $^3J_{HH}$ = 8.76, $^3J_{HH}$ = 7.15, $^4J_{HH}$ = 1.47 Hz, 1H), 8.11–8.00 (m, 3H), 7.77–7.58 (m, 3H), 6.25 (s, 2H), 4.26 (q, J = 7.10 Hz, 2H), 1.26 (t, J = 7.10 Hz, 3H). ^{13}C-NMR (75 MHz, DMSO-d_6) δ 166.35, 166.18, 145.56, 136.63, 135.54, 134.68, 133.54, 132.97, 130.44, 130.31, 129.38, 128.95, 128.01, 118.75, 62.63, 58.10, 14.00. MS (ESI$^+$) m/z = 334.7, Calcd. [$C_{20}H_{19}N_2O_3^+$ = 335.1]. IR (ATR) 3411.51*w* (N–H), 3029.37*w* (C–H, arom.), 2951.74*w* (C–H), 1748.19*m* (C═O), 1673.64*m* (N–H), 1570.51*m* (N–H), 1374.45*m* (–CH_3), 1289.56*m* (C–N), 1208.84*m* (C–O). Anal. Calcd. For $C_{20}H_{19}BrN_2O_3$: C, 57.84; H, 4.61; N, 6.75. Found: C, 57.53; H, 4.77; N, 6.54.

Crystallographic investigations

The crystallographic data, refinement details and hydrogen bonds parameters for **1** and **2** are summarized in Tables S1–S3.† Data for all compounds were collected on a Bruker APEX II CCD diffractometer at 100 K; using MoK_α radiation (k = 0.71073 Å) from an Incoatec ImuS source and a Helios optic monochromator.[73] Suitable crystals were coated with hydrocarbon oil,

Open Access Article. Published on 29 2022. Downloaded on 03-08-2025 12:06:24.
This article is licensed under a Creative Commons Attribution-NonCommercial 3.0 Unported Licence.

picked up with a nylon loop, and mounted in the cold nitrogen stream of the diffractometer. The structures were solved using intrinsic phasing (SHELXT) and refined by full-matrix least-squares on F^2 using the ShelXle GUI.[74,75] The hydrogen atoms of the C–H bonds were placed in idealized positions whereas the hydrogen atoms from the O–H moieties and hydrogens for water were localized from the difference electron density map and fixed to standard distances using DFIX instructions, and their position was refined with U_{iso} tied to the parent atom with distance restraints. CCDC 2118468–2118469 contain the ESI† crystallographic data for this paper. These data can be obtained free of charge from The Cambridge Crystallographic Data Centre *via* **www.ccdc.cam.ac.uk/datarequest/cif**.

Fluorimetric titration experiments

Titration experiments were performed by adding aliquots of stock solutions of NPPs to a buffered aqueous solution containing MOPS (10 mM, pH = 7.0) of **1** (15 μM). In all these experiments the ionic strength was adjusted to 0.05 M with NaCl. After addition of NPPs, the solution was equilibrated for 1 min. at r. t. before recording the emission spectrum ($\lambda_{ex} = 350$ nm) using a 10 mm quartz cuvette. The experimental data were fitted to corresponding eqn (1) using non-linear least-squares regression with Microcal Origin 8.1 for 1 : 1 model. The selectivity experiments were performed by adding aliquots of stock solutions of the respective sodium salts of NPPs ($[NPPs]_{final}$ = 0.5 mM) to buffered aqueous solutions containing MOPS at pH = 7.0 of **1** (15 μM) and the emission intensities at 415 nm were recorded. All spectrophotometric experiments were performed in triplicate, and the mean values are reported.

Spectrophotometric, ^{1}H and ^{31}P NMR titration experiments

The absorption spectra were recorded after additions of aliquots of ATP stock solution to a buffered (10 mM, MOPS at pH = 7.0 and ionic strength of 0.05 M NaCl) aqueous solutions of **1** (40 μM) in a quartz cuvette placed in a compartment Cary 100 Agilent spectrophotometer thermostated at 25 ± 0.1 °C with a recirculating water bath. ^{1}H NMR titration experiments were performed on a 400 MHz spectrometer at 25 °C in D_2O, adding aliquots with more concentrated stock solutions of sodium salts of ATP or GTP in D_2O adding aliquots of them to solutions of **1** (2.0 mM) directly to NMR tubes. For ^{31}P NMR experiments, the spectra were recorded at 121.5 MHz using H_3PO_4 as external standard.

Computational details

The geometry optimizations of corresponding 1 : 1 complexes between nucleoside triphosphates and **1** were carried out with the Grimme's three-fold corrected (3c) composite method PBEh-3c. This methodology shows excellent performance for non-covalent interaction energies in small and large complexes.[76] All structures were confirmed as a minimum of energy according to a no-imaginary frequencies criteria. Interaction energy, E_{int}, was corrected due to solvent effect using the implicit solvation model CPCM,[77] with water as solvent and calculated using the classical reaction model: $E_{int} = E_{complex} - (E_{ligand} + E_{B3QR})$, were $E_{complex}$ refer to the energy of 1 : 1 complex and E_{ligand} and E_{B3QR} refer to energy of ligand and receptor respectively. Non-Covalent-Interactions-Index, NCI, was used for inter-molecular interactions analysis. All calculations were carried out with orca 4.2.0,[78] while Multiwfn 3.8 (ref. 79) was used for NCI analysis.[80]

Competitive displacement assays by fluorescence spectroscopy

A stock solution of salmon sperm DNA was prepared by dissolving 5.0 mg in 10 ml of buffered aqueous solution (5.0 mM Tris–HCl and 50.0 mM NaCl) at pH 7.0. A ratio of UV absorbance A280 of 1.86 indicated that DNA was sufficiently free from protein. The DNA concentration was calculated by UV spectrophotometry, using the molar absorption coefficient 6600 M^{-1} cm^{-1} at 260 nm.[72] The stock solution was diluted accordingly to obtain a 1.0 mM working solution. **1** was dissolved in pure DMSO at stock concentrations of 5.0 mM. To get insight the interaction between **1** and DNA, an ethidium bromide competitive assay was performed. The experiments were carried out in neutral buffered aqueous solutions (5.0 mM Tris–HCl and 50.0 mM NaCl) using a 1.0 cm cuvette containing fixed final concentration of DNA–EB at 250 μM and 50 μM, respectively. This solution was titrated with a concentrated solution of **1**. After the addition of the aliquots, the sample was mixed and allowed to equilibrate for 3 min and the fluorescence spectra were recorded at 25 or 37 °C ($\lambda_{ex} = 520$ nm).

All fluorescence intensities were corrected by the equation; $I_{cor} = I_{obs}e^{(Aex+Aem)/2}$, where I_{cor} and I_{obs} are the corrected and observed intensities, A_{ex} and A_{em} are the absorbances of **1** at excitation and emission wavelengths.

Molecular dynamics simulation

The AMBER Molecular Dynamics engine (MD) was used to study the interaction of **1** with the double stranded DNA with the sequence: d (CATGCATGCATGCATGCATCATGCATG) built with the DS Visualizer. The structure was solvated with the Optimum Point Charge (OPC)[81] water model and NaCl ions were added at a 200 mM concentration to neutralize the charge using the Joung–Cheatham model[82] in a truncated octahedron unit cell. Compound **1** was described by the General Amber Force Field[83] with the charges calculated using the RESP methodology. Three compounds where manually incorporated to the DNA model and the entire system was minimized using the protocol described by Roe.[84] Double stranded DNA was described by the OL15(ref. 85) optimized force field and three independent replicas where run using the GPU PMEMD code.[86] Analysis was performed using CPPTRAJ[87] as available in AmberTools.

Conflicts of interest

There are no conflicts to declare.

Acknowledgements

We thank Chem. Eréndira García Rios, Chem María P. Orta Pérez, Chem. M. Angeles Peña González, M. Sc. Lucero M. Ríos

© 2022 The Author(s). Published by the Royal Society of Chemistry

Ruiz, M. Sc. L. Carmen Márquez Alonso, M. Sc. Elizabeth Huerta Salazar, Dra. Adriana Romo Pérez and Dra. Beatriz Quiroz García for technical assistance. We thank PAPIIT-UNAM-216220 and CONACYT PRONACES-160671 for financial support. A. O. V.-P., R. V. V.-C. and M. K., S.-F. is grateful to CONACyT for scholarship 868013, 688503 and 848759 respectively and U. R.-M. is grateful to PAPIIT for scholarship 120121. We thank the LANCAD and the Laboratory of Supercomputer at the UAM-Iztapalapa for access to its computer facilities.

Open Access Article. Published on 29 2022. Downloaded on 03-08-2025 12:06:24.
This article is licensed under a Creative Commons Attribution-NonCommercial 3.0 Unported Licence.

References

1 S. E. Bodman and S. J. Butler, *Chem. Sci.*, 2021, **12**, 2716–2734.
2 D. A. McNaughton, M. Fares, G. Picci, P. A. Gale and C. Caltagirone, *Coord. Chem. Rev.*, 2021, **427**, 213573.
3 M. Pushina, S. Farshbaf, W. Mochida, M. Kanakubo, R. Nishiyabu, Y. Kubo and P. Anzenbacher, *Chem.–A Eur. J.*, 2021, **27**, 11344–11351.
4 S. H. Hewitt, G. Macey, R. Mailhot, M. R. J. Elsegood, F. Duarte, A. M. Kenwright and S. J. Butler, *Chem. Sci.*, 2020, **11**, 3619–3628.
5 R. V. Velázquez-Castillo, M. K. Salomón-Flores, A. O. Viviano-Posadas, I. J. Bazany-Rodríguez, C. Bustos-Brito, J. M. Bautista-Renedo, N. González-Rivas, L. D. Rosales-Vázquez and A. Dorazco-González, *Dyes Pigm.*, 2021, **196**, 109827.
6 S. Mishra, S. M. Hossain and A. K. Singh, *Spectrochim. Acta, Part A*, 2020, **240**, 118600.
7 A. M. Agafontsev, A. Ravi, T. A. Shumilova, A. S. Oshchepkov and E. A. Kataev, *Chem.–A Eur. J.*, 2019, **25**, 2684–2694.
8 R. L. P. Adams, J. T. Knowler and D. P. Leader, *The Biochemistry of the Nucleic Acids*, Springer Netherlands, Dordrecht, 1986.
9 Y. Zhou, Z. Xu and J. Yoon, *Chem. Soc. Rev.*, 2011, **40**, 2222.
10 S. Shoji, S. E. Walker and K. Fredrick, *ACS Chem. Biol.*, 2009, **4**, 93–107.
11 P. Bhargava and R. G. Schnellmann, *Nat. Rev. Nephrol.*, 2017, **13**, 629–646.
12 G. Burnstock, *Trends Pharmacol. Sci.*, 2006, **27**, 166–176.
13 J. Downward, *Nat. Rev. Cancer*, 2003, **3**, 11–22.
14 H. Tao, L. He, G. Cheng and Q.-Y. Cao, *Dyes Pigm.*, 2019, **166**, 233–238.
15 S. Dey, T. Sarkar, A. Majumdar, T. Pathak and K. Ghosh, *ChemistrySelect*, 2017, **2**, 2034–2038.
16 A. K. Gupta, A. Dhir and C. P. Pradeep, *Eur. J. Org. Chem.*, 2015, **2015**, 122–129.
17 L. S. Mittal, P. Sharma, N. Kaur and P. Singh, *Anal. Methods*, 2019, **11**, 5320–5327.
18 N. Wu, J. Lan, L. Yan and J. You, *Chem. Commun.*, 2014, **50**, 4438–4441.
19 N. Ahmed, B. Shirinfar, I. S. Youn, M. Yousuf and K. S. Kim, *Org. Biomol. Chem.*, 2013, **11**, 6407–6413.
20 N. Ahmed, B. Shirinfar, I. S. Youn, A. Bist, V. Suresh and K. S. Kim, *Chem. Commun.*, 2012, **48**, 2662–2664.
21 S. K. Kim, B.-S. Moon, J. H. Park, Y. Il Seo, H. S. Koh, Y. J. Yoon, K. D. Lee and J. Yoon, *Tetrahedron Lett.*, 2005, **46**, 6617–6620.
22 H. N. Kim, J. H. Moon, S. K. Kim, J. Y. Kwon, Y. J. Jang, J. Y. Lee and J. Yoon, *J. Org. Chem.*, 2011, **76**, 3805–3811.
23 W. Lang, G. Cheng, R. Peng and Q.-Y. Cao, *Dyes Pigm.*, 2021, **189**, 109245.
24 N. H. Kim, B. W. Kim, H. Moon, H. Yoo, R. H. Kang, J. K. Hur, Y. Oh, B. M. Kim and D. Kim, *Anal. Chim. Acta*, 2021, **1152**, 338269.
25 H. Y. Kuchelmeister and C. Schmuck, *Chem.–A Eur. J.*, 2011, **17**, 5311–5318.
26 S. C. Karunakaran, A. K. Paul and D. Ramaiah, *RSC Adv.*, 2014, **4**, 30644–30647.
27 S. Farshbaf and P. Anzenbacher, *Chem. Commun.*, 2019, **55**, 1770–1773.
28 X. Zhang, J. Liu, J. Wang, L. Han, S. Ma, M. Zhao and G. Xi, *J. Photochem. Photobiol., B*, 2021, **223**, 112279.
29 A. M. Agafontsev, T. A. Shumilova, A. S. Oshchepkov, F. Hampel and E. A. Kataev, *Chem.–A Eur. J.*, 2020, **26**, 9991–9997.
30 R. M. Duke, T. McCabe, W. Schmitt and T. Gunnlaugsson, *J. Org. Chem.*, 2012, **77**, 3115–3126.
31 S. Kubik, *Chem. Soc. Rev.*, 2010, **39**, 3648.
32 I. J. Bazany-Rodríguez, M. K. Salomón-Flores, J. M. Bautista-Renedo, N. González-Rivas and A. Dorazco-González, *Inorg. Chem.*, 2020, **59**, 7739–7751.
33 A. E. Hargrove, S. Nieto, T. Zhang, J. L. Sessler and E. V. Anslyn, *Chem. Rev.*, 2011, **111**, 6603–6782.
34 H. Chen, Z. Zhou, Z. Li, X. He and J. Shen, *Spectrochim. Acta, Part A*, 2021, **257**, 119792.
35 D. Maity, M. Li, M. Ehlers and C. Schmuck, *Chem. Commun.*, 2017, **53**, 208–211.
36 P. Sun, H. Zhang, Y. Sun and J. Liu, *Spectrochim. Acta, Part A*, 2021, **245**, 118919.
37 J. Lohrman, S. Pramanik, S. Kaur, H. Telikepalli, V. W. Day and K. Bowman-James, *Org. Biomol. Chem.*, 2021, **19**, 8516–8520.
38 A. Dorazco-González, M. F. Alamo, C. Godoy-Alcántar, H. Höpfl and A. K. Yatsimirsky, *RSC Adv.*, 2014, **4**, 455–466.
39 C. D. Geddes, K. Apperson, J. Karolin and D. J. Birch, *Anal. Biochem.*, 2001, **293**, 60–66.
40 A. Dorazco-González, H. Höpfl, F. Medrano and A. K. Yatsimirsky, *J. Org. Chem.*, 2010, **75**, 2259–2273.
41 R. Badugu, *Dyes Pigm.*, 2004, **61**, 227–234.
42 X. Xie, O. Reznichenko, L. Chaput, P. Martin, M.-P. Teulade-Fichou and A. Granzhan, *Chem.–Eur. J.*, 2018, **24**, 12638–12651.
43 C. Miron and A. Petitjean, *Synlett*, 2018, **29**, 1362–1366.
44 B.-X. Zheng, W. Long, Y.-H. Zhang, X.-H. Huang, C.-C. Chen, D.-X. Zhong, M.-T. She, Z.-X. Chen, D.-P. Cai, Y.-J. Lu and W.-L. Wong, *Sens. Actuators, B*, 2020, **314**, 128075.
45 V. Dhamodharan, S. Harikrishna, C. Jagadeeswaran, K. Halder and P. I. Pradeepkumar, *J. Org. Chem.*, 2012, **77**, 229–242.

© 2022 The Author(s). Published by the Royal Society of Chemistry

Open Access Article. Published on 29 2022. Downloaded on 03-08-2025 12:06:24.
This article is licensed under a Creative Commons Attribution-NonCommercial 3.0 Unported Licence.

46 M. D. Gray, P. S. Deore, A. J. Chung, A. J. Van Riesen, R. A. Manderville, P. S. Prabhakar and S. D. Wetmore, *Bioconjugate Chem.*, 2020, **31**, 2596–2606.
47 I. J. Bazany-Rodríguez, D. Martínez-Otero, J. Barroso-Flores, A. K. Yatsimirsky and A. Dorazco-González, *Sens. Actuators, B*, 2015, **221**, 1348–1355.
48 T. Ema, K. Okuda, S. Watanabe, T. Yamasaki, T. Minami, N. A. Esipenko and P. Anzenbacher, *Org. Lett.*, 2014, **16**, 1302–1305.
49 S.-O. Kang, T. S. Johnson, V. W. Day and K. Bowman-James, *Supramol. Chem.*, 2018, **30**, 305–314.
50 H. Goyal, S. Pachisia and R. Gupta, *Cryst. Growth Des.*, 2020, **20**, 6117–6128.
51 P. Kumar, V. Kumar, S. Pandey and R. Gupta, *Dalton Trans.*, 2018, **47**, 9536–9545.
52 P. Kumar, V. Kumar and R. Gupta, *Dalton Trans.*, 2020, **49**, 9544–9555.
53 P. Molina, F. Zapata and A. Caballero, *Chem. Rev.*, 2017, **117**, 9907–9972.
54 M. Nicolas-Gomez, I. J. Bazany-Rodríguez, E. Plata-Vargas, S. Hernández-Ortega and A. Dorazco-González, *Acta Crystallogr., Sect. E: Crystallogr. Commun.*, 2016, **72**, 747–750.
55 W. F. Jager, T. S. Hammink, O. van den Berg and F. C. Grozema, *J. Org. Chem.*, 2010, **75**, 2169–2178.
56 K. Tanabe, Y. Suzui, M. Hasegawa and T. Kato, *J. Am. Chem. Soc.*, 2012, **134**, 5652–5661.
57 Y. Fuentes-Martínez, C. Godoy-Alcántar, F. Medrano, A. Dikiy and A. K. Yatsimirsky, *Supramol. Chem.*, 2010, **22**, 212–220.
58 J. A. Roberts and R. J. Evans, *J. Biol. Chem.*, 2004, **279**, 9043–9055.
59 V. Amendola, L. Fabbrizzi and E. Monzani, *Chem.–Eur. J.*, 2004, **10**, 76–82.
60 E. Novikov and N. Boens, *J. Phys. Chem. A*, 2007, **111**, 6054–6061.
61 K. Ghosh and I. Saha, *New J. Chem.*, 2011, **35**, 1397–1402.
62 K. Ghosh and I. Saha, *Org. Biomol. Chem.*, 2012, **10**, 9383–9392.
63 S. Dey, T. Sarkar, A. Majumdar, T. Pathak and K. Ghosh, *ChemistrySelect*, 2017, **2**, 2034–2038.
64 O. Sunnapu, N. G. Kotla, B. Maddiboyina, S. Marepally, J. Shanmugapriya, K. Sekar, S. Singaravadivel and G. Sivaraman, *ChemistrySelect*, 2017, **2**, 7654–7658.
65 K.-Y. Tan, C.-Y. Li, Y.-F. Li, J. Fei, B. Yang, Y.-J. Fu and F. Li, *Anal. Chem.*, 2017, **89**, 1749–1756.
66 K. Ghosh, D. Tarafdar, A. Samadder and A. R. Khuda-Bukhsh, *RSC Adv.*, 2015, **5**, 35175–35180.
67 M. Sirajuddin, S. Ali and A. Badshah, *J. Photochem. Photobiol., B*, 2013, **124**, 1–19.
68 Y. Sun, S. Bi, D. Song, C. Qiao, D. Mu and H. Zhang, *Sens. Actuators, B*, 2008, **129**, 799–810.
69 E. Oguzcan, Z. Koksal, T. Taskin-Tok, A. Uzgoren-Baran and N. Akbay, *Spectrochim. Acta, Part A*, 2022, **270**, 120787.
70 *Principles of Fluorescence Spectroscopy*, ed., J. R. Lakowicz, Springer US, Boston, MA, 2006.
71 S. Ozkan, T. Taskin-Tok, A. Uzgoren-Baran and N. Akbay, *J. Fluoresc.*, 2019, **29**, 101–110.
72 J. Valdes-García, A. O. Viviano-Posadas, J. Rivera-Chávez, T. Ramírez-Apan, S. Martínez-Vargas, E. Aguirre-Hernández, J. M. German-Acacio, D. Morales-Morales and A. Dorazco-González, *J. Mol. Struct.*, 2022, **1249**, 131582.
73 *APEX 2 Softw. Suite*, Bruker AXS Inc., Madison, Wisconsin, USA, 2004.
74 C. B. Hübschle, G. M. Sheldrick and B. Dittrich, ShelXle: A Qt graphical user interface for SHELXL, *J. Appl. Crystallogr.*, 2011, **44**, 1281–1284.
75 G. M. Sheldrick, SHELXT - Integrated space-group and crystal-structure determination, *Acta Crystallogr., Sect. C: Struct. Chem.*, 2015, **71**, 1–8.
76 S. Grimme, J. G. Brandenburg, C. Bannwarth and A. Hansen, *J. Chem. Phys.*, 2015, **143**, 054107.
77 Y. Takano and K. N. Houk, *J. Chem. Theory Comput.*, 2005, **1**, 70–77.
78 F. Neese, F. Wennmohs, U. Becker and C. Riplinger, *J. Chem. Phys.*, 2020, **152**, 224108.
79 T. Lu and F. Chen, *J. Comput. Chem.*, 2012, **33**, 580–592.
80 J. Contreras-García, E. R. Johnson, S. Keinan, R. Chaudret, J.-P. Piquemal, D. N. Beratan and W. Yang, *J. Chem. Theory Comput.*, 2011, **7**, 625–632.
81 Y. Xiong, P. S. Shabane and A. V. Onufriev, *ACS Omega*, 2020, **5**, 25087–25094.
82 I. S. Joung and T. E. Cheatham, *J. Phys. Chem. B*, 2008, **112**, 9020–9041.
83 J. Wang, R. M. Wolf, J. W. Caldwell, P. A. Kollman and D. A. Case, *J. Comput. Chem.*, 2004, **25**, 1157–1174.
84 D. R. Roe and B. R. Brooks, *J. Chem. Phys.*, 2020, **153**, 054123.
85 R. Galindo-Murillo, J. C. Robertson, M. Zgarbová, J. Šponer, M. Otyepka, P. Jurečka and T. E. Cheatham, *J. Chem. Theory Comput.*, 2016, **12**, 4114–4127.
86 A. W. Götz, M. J. Williamson, D. Xu, D. Poole, S. Le Grand and R. C. Walker, *J. Chem. Theory Comput.*, 2012, **8**, 1542–1555.
87 D. R. Roe and T. E. Cheatham, *J. Chem. Theory Comput.*, 2013, **9**, 3084–3095.

© 2022 The Author(s). Published by the Royal Society of Chemistry